Nonlinear vertical accelerations of a floating torus in regular waves

Peng Li[a,*], Odd M. Faltinsen[a], Claudio Lugni[a,b]

[a] *Centre for Autonomous Marine Operations and Systems (AMOS), Department of Marine Technology, NTNU, NO-7491Trondheim, Norway*
[b] *CNR-INSEAN Italian Ship Model Basin, Via di Vallerano 139, 00128 Roma, Italy*

Abstract

The longitudinal motions and vertical accelerations of a floating torus as well as wave motion inside the torus are studied by model tests in regular deep-water waves. Comparisons are made with linear and partly with second-order potential-flow theory for the smallest examined experimental wave height-to-wave length ratio 1/120. Reasonable agreement is obtained, in particular for the linear problem. The importance of 3D flow, hydroelasticity and strong hydrodynamic frequency dependency is documented. Experimental precision errors and bias errors, for instance, due to tank-wall interference are discussed. Numerical errors due to viscous effects are found to be secondary. Experiments show that the third and fourth harmonic accelerations of the torus matter and cannot be explained by a perturbation method with the wave steepness as a small parameter.

Keywords: Model tests, Boundary Element Method, Waves, Torus, Nonlinear response, Error analysis

1. Introduction

Wave-induced loads on a fish farm with a circular plastic collar motivate our studies. The interaction with other parts of the fish farm, such as the netting structure, bottom rings, chains, ropes and a realistic mooring system, are important but are not investigated. Both wave and current loads matter but current is neglected. Dynamic behavior of a fish farm in real conditions is a complex scenario (see Figure 1), which for the floater can involve large relative vertical motion compared to the cross-sectional dimensions, large local accelerations, hydroelastic effects and violent wave structure interaction with local wave overtopping and out of water phenomena.

Dedicated model tests and numerical simulations by Kristiansen and Faltinsen (2015) investigated the mooring loads through a detailed and broad numerical study and assessed the physical effects which are relevant for the prediction of the mooring loads. Amongst them, a rigid floater significantly alters the mooring loads if compared with a realistic elastic

*Corresponding author. Tel.: +47 463 61 524
Email address: peng.li@ntnu.no (Peng Li)

Figure 1: Illustrations of overtopping and out of water on the floater of a fish farm without net in a storm. (Photo: Marius Dahle Olsen)

floater. He et al. (2015) demonstrated by model tests with live fish occupying a representative volume 2.5% of the net cage that fish could have a non-negligible influence on the mooring loads in waves and current.

The considered floater is a torus even though it is more common in practice to operate with two adjacent tori. Wavelengths of practical interest are of the order of the torus diameter but long relative to the cross-sectional diameter. Engineering tools for net cages often estimate the wave-induced floater loads using strip theory with linear potential flow and drag-force corrections from Morison equation, which disregard important 3D flow, frequency dependency and nonlinear effects.

Newman (1977) analyzed a rigid floating torus by linear potential flow. Li and Faltinsen (2012) derived a long wavelength slender-body theory for the vertical added mass, damping and wave excitation loads on an elastic semi-submerged torus by matching a near-field and far-field solution. Here long wavelength means that the wavelength is long relative to the cross-sectional torus diameter. A Haskind-type expression for the wave excitation loads was presented. 3D frequency-dependent hydrodynamic interaction on the scale of the torus diameter was significant and resulted, for instance, in frequencies with zero wave-radiation damping. A beam model described the elasticity effect of the torus and a representative bending stiffness for the floater of a fish farm was applied. Hydroelasticity played a major role in the studied cases. The results were verified by complete 3D linear frequency-domain potential-flow calculations.

Li et al. (2014) reported numerical simulations and experiments of an elastic circular collar of a floating fish farm. The floater model without netting structure and moored with nearly horizontal moorings were tested in regular deep-water waves of different steepness and periods without current. Local overtopping of waves were observed in steep waves. The focus was on the vertical accelerations along the floater in different conditions. The experiments

showed that higher-order harmonics of the accelerations are significant. A 3D weak-scatter model with partly nonlinear effects due to Froude-Kriloff and unsteady hydrostatic pressure loads as well as a 3D linear frequency-domain method based on potential flow were used. From their comparison against the measurements, strong 3D and frequency dependency effects as well as flexible floater motions matter. The weak-scatter model can only partly explain the nonlinearities present in the measured accelerations.

The present experimental investigation is a continuation of the experimental work by Li et al. (2014) by considering a nearly rigid circular floater. In that way, state-of-the-art second-order potential flow solvers for rigid bodies is used to explain some of the nonlinear experimental results. In the next section the model tests are outlined, then the adopted numerical solvers and the applied elastic curved-beam theory are briefly described and the physical investigation is discussed. Emphasis is given on the discussion of experimental and theoretical error sources. Main conclusions and further steps are drawn in the last section.

2. Experimental set-up

The Marine Cybernetics Laboratory at the Marine Technology Centre in Trondheim was used for the experiments. The wave tank is $40m$ long, $6.45m$ wide and $1.5m$ deep. It is equipped with a towing carriage, a hinged flap-type wave maker and a damping beach covered by a porous mat to increase its energy dissipation ability. The wave maker is digitally controlled by using linear wave maker theory to estimate the necessary stroke of the paddle for generating waves with a given height and period. A scale factor $1:25$ with Froude scaling was in mind for the floater model. In order to get a cross-sectional diameter similar to the one used for the elastic model in Li et al. (2014), *i.e.* $36mm$, a $32mm$ nearly rigid standard water pipe for houses was covered by a transparent elastic tube of thickness $1.5mm$ and a waterproof adhesive electrical tape. The water pipe is made of a high-density polyethylene (HDPE) type plastic with Young's modulus of elasticity $E = 0.8 \times 10^9 N/m^2$. The second moment of area of the pipe in bending is $I = \pi \left(D_2^4 - D_1^4\right)/64$, where the inner and outer diameter are $D_1 = 26mm$ and $D_2 = 32mm$, respectively. This means a bending stiffness $EI = 23.23Nm^2$. The combined bending stiffness of the HDPE plastic tube, transparent elastic tube and the adhesive electrical tape was found by static tests in the linear elastic regime. An arc of the torus was clamped to one end and kept free on the other and an increasing load, whose range was comparable with the one recorded during the tests in waves, has been applied on the free end and the corresponding displacement has been measured. The static tests confirmed the linear behaviour of the material and enabled the calculation of the bending stiffness $EI = 23.74Nm^2$, that is, about 200 times the bending stiffness used in the experiments by Li et al. (2014). The yield stress ($23°\mathrm{C}, 50mm/min$) of the pipe is $22MPa$. The largest moment in the torus due to the dominant elastic mode is about $10.3Nm$. So, the largest stress in the cross-section is $6.2MPa$, which is much smaller than the yield stress.

The experimental set-up is illustrated in Figure 2. The Earth-fixed Cartesian coordinate system $Oxyz$ is also defined in Figure 2 with the mean free surface at $z = 0$. The z-axis is the torus axis and upwards. The diameter of the torus-shaped floater measured to the

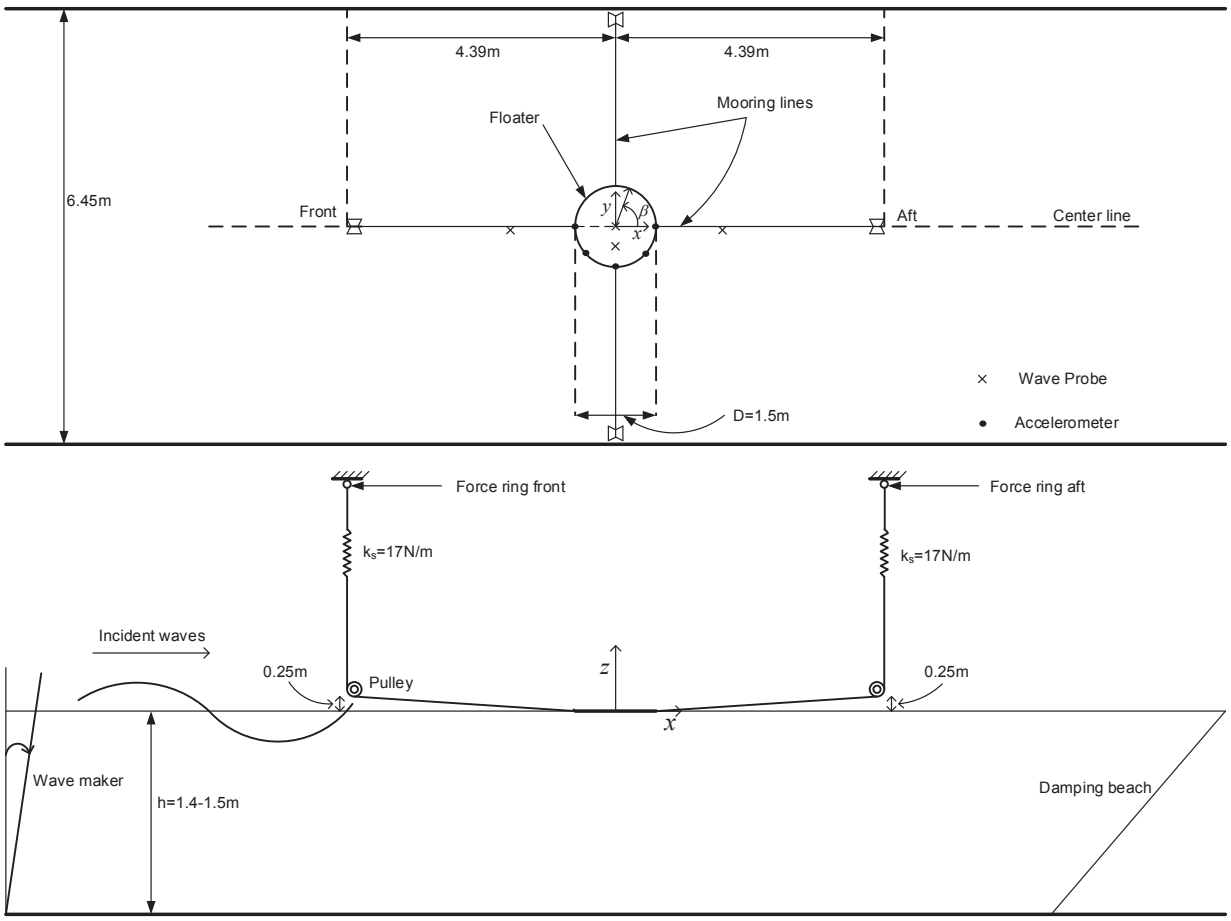

Figure 2: Experimental set-up. Upper: top view; lower: side view. The damping beach is out of scale. Definition of Earth-fixed coordinate system $Oxyz$ and angle β.

center of the torus cross-section is $D = 2c = 1.5m$. The cross-sectional torus diameter and mass of the floater are $2a = 0.036m$ and $2.86kg$, respectively. The draft of the floater is $0.0214m$. The floater was attached to the stationary carriage in the middle of the tank by means of four identical nearly horizontal mooring lines, at front, aft, left and right. Springs with stiffness $k_s = 17N/m$ were used to connect the floater to the carriage. This corresponds to almost half of the full scale spring stiffness ($27kN/m$) by Froude scaling. The pre-tension was $T_p = 5N$. The high pre-tension was needed to avoid slack due to large horizontal motion when testing large wave steepness and long wave periods.

Finally two cameras were used to record the global behaviour of the floater and the accuracy of overtopping and out-of-water phenomena. One camera is underwater with a frame rate of $25fps$ and a resolution of 768×576 pixel. The second, in air and almost perpendicular to the free surface plane has a frame rate of $25fps$ and a resolution of 1920×1080 pixel.

No experimental free-decay tests were done to identify wet natural periods and damping. Such tests are difficult to perform because the strong frequency dependency of added mass

causes several natural frequencies for the dominant modes, *i.e.* heave, pitch and the lowest vertical elastic mode. The theoretical nine lowest undamped natural frequency for uncoupled heave, pitch and the lowest vertical elastic mode are presented in Table 1. They are higher than the experimental frequency range of the linear incident regular waves. The theoretical undamped natural frequency in uncoupled surge due to the mooring system is $2.17 rad/s$, which is clearly smaller than the experimental frequency range.

Heave	22.63	23.49	24.35	25.17	25.97	26.37	26.89	27.65	28.39
Pitch	23.07	23.93	24.75	25.57	26.34	26.51	27.27	28.01	28.75
The lowest purely vertical elastic mode	33.08	33.70	34.30	34.89	35.47	36.05	36.61	37.17	37.73

Table 1: The nine lowest numerically predicted undamped natural frequencies in rad/s for the dominant vertical modes.

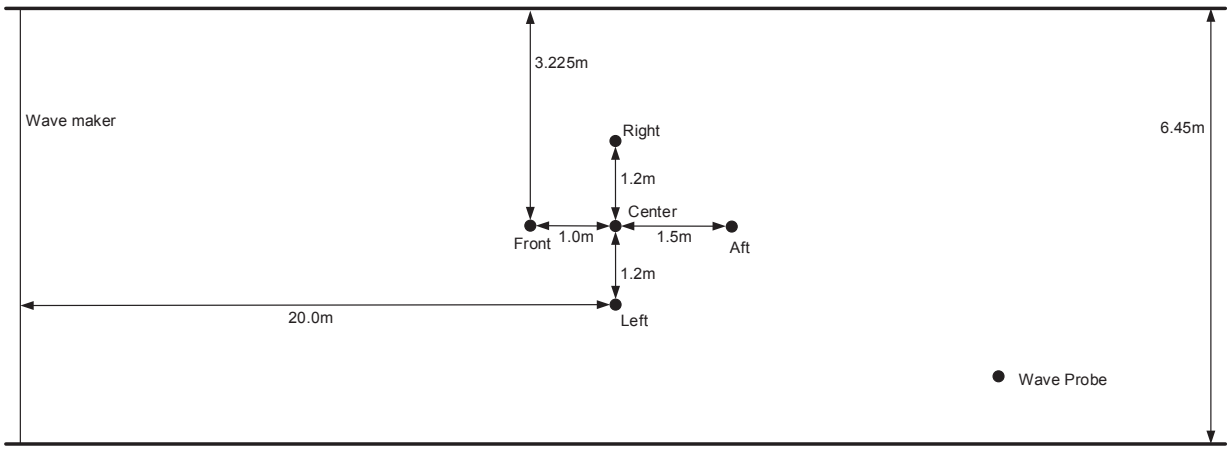

Figure 3: Top view of experimental set-up for wave measurements without the torus present.

2.1. Check of the wave generation

To estimate the error in the generation of the incident regular wave system with respect to the nominal values, tests without the torus in the tank have been carried out. Incident waves with prescribed wave height-to-wave length ratios $H/\lambda = 1/120, 1/60, 1/30$ and $1/15$ propagating along the x-axis were tested. The wave period $T = 2\pi/\omega$ varied within $[0.6, 1.6]\, s$ with a step of $0.05s$. Here ω is the circular frequency. Five resistance wave probes with wire diameter $3mm$ were positioned as illustrated in Figure 3. The waiting time between each test was $4 - 5$ minutes. Each test was repeated $2 - 3$ times showing good repeatability. A zoomed view of the ratio between the measured first harmonic component and the nominal wave amplitude is shown in Figure 4 for the different prescribed wave steepness as function of the non-dimensional wave number νa where $\nu = \omega^2/g$ with g meaning acceleration of

gravity. The mean values and the corresponding standard deviations, estimated through the time histories of the five wave probes, are reported. Possible reasons to the disagreement between measured and nominal wave amplitude are wave reflections from the beach, meniscus effect on the wave probe wire, calibration linearity error and nonlinear effects in the wave propagation.

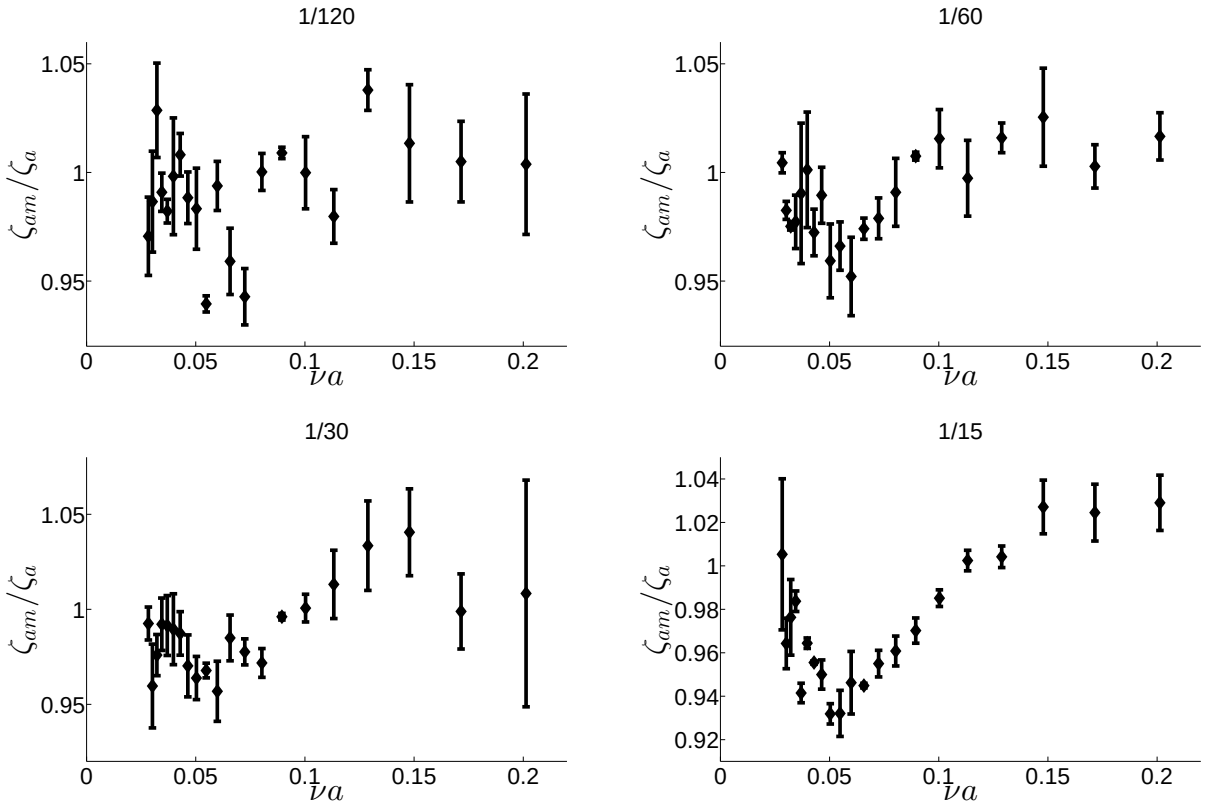

Figure 4: Zoomed view of ratio between measured and prescribed wave amplitude versus non-dimensional wave number νa without the torus present. ζ_{am} is the mean wave amplitude of the five measurement positions in Figure 3. ζ_a is the prescribed wave amplitude. The height of the experimental error bars is two times the estimated standard deviation. The numbers $1/120, 1/60, 1/30$ and $1/15$ on the top of each graph is the prescribed wave steepness.

2.2. Torus acceleration measurements

Accelerations were measured along the body-fixed $\overline{z}$-axis, which coincides with the vertical z-axis when the torus is at rest. Five positions along the torus corresponding to the angles $\beta = 0, \pi/4, \pi/2, 3\pi/4, \pi$ as defined in Figure 2 were used. They are referred to as aft, aft left, left, front left and front positions, respectively. The used accelerometers were Model $3032-050$ by Measurement Specialists, with a sensitivity of $1.318mV/g$. All test cases were repeated $2-3$ times, in order to check their repeatability: a maximum repeatability error of about 1.0% was assessed. A waiting time of 3 minutes between two consecutive tests was

chosen to get almost calm water conditions. The time recording started 20 seconds earlier than the wave maker to ensure the acquisition of the longitudinal seiching mode effect, as well as of the residual waves generated in the previous test. In particular, when a small difference in the period between the previous and the actual incident waves exists, weak beating effect arises in the actual time history of the torus motions. Possible drift in the accelerometers was detected before the wave maker started and used to correct the signal in the subsequent run.

In general, nearly steady-state oscillations are reached after 10 wave periods. The steady-state time window were band-pass filtered in order to remove noise out of the prescribed frequency range. The lower and upper cut-off frequencies are $0.95/T$ and $1.05/T$, $1.95/T$ and $2.05/T$, $2.95/T$ and $3.05/T$, $3.95/T$ and $4.05/T$ in order to get first, second, third and fourth-order harmonics of acceleration, respectively. The sampling frequency was $100Hz$. The steady-state time window contained about $70 - 130$ wave periods. A sliding Discrete Fourier Transform (DFT) technique is used to determine the time variation of each harmonic contribution. A time window corresponding to 20 wave periods is analyzed through DFT; then the time window is slid one wave period and the DFT analysis is repeated for the new time interval. The procedure is repeated until the end of the steady-state region, enabling the evaluation of the mean value and standard deviation of each harmonic component. A second method was used to calculate mean values and standard deviation. It is based on the envelope curve of the absolute values of the acceleration extrema (maxima and minima) in the same steady-state time window. The corresponding mean and standard deviation values are used as the measurements of the mean value and error estimation. Mean values obtained by the two methods are very close, however differences on the standard deviations are significant.

Large relative vertical motions with waves overtopping the floater locally and local out-of-water effect of the floater were observed in the model scale experiments (see Figure 5 and attached movie). Similar phenomena are demonstrated in Figure 1 for the floater of a fish farm without netting in a storm. Overtopping occurs for all wave periods with wave height-to-wavelength ratio 1/15 and for wave periods larger than $T = 1.05s$ with wave height-to-wavelength ratio 1/30 (see Figure 5). There is no overtopping occurring for wave height-to-wavelength ratio 1/60 and 1/120. To properly examine the nonlinear features of the phenomena, first, second, third and fourth-order harmonics of the measured acceleration signals were estimated. Harmonics higher than fourth-order were small.

2.3. Longitudinal and transverse motion measurements

The longitudinal motions of the torus were determined by using the mooring load registrations at the front and aft positions of floater together with the known stiffness ($k_s = 17N/m$) of the springs. The transverse motions were similarly estimated by using the mooring load registrations at the left and right floater positions. The time series were analyzed as described above for the vertical accelerations by considering only the first harmonic part.

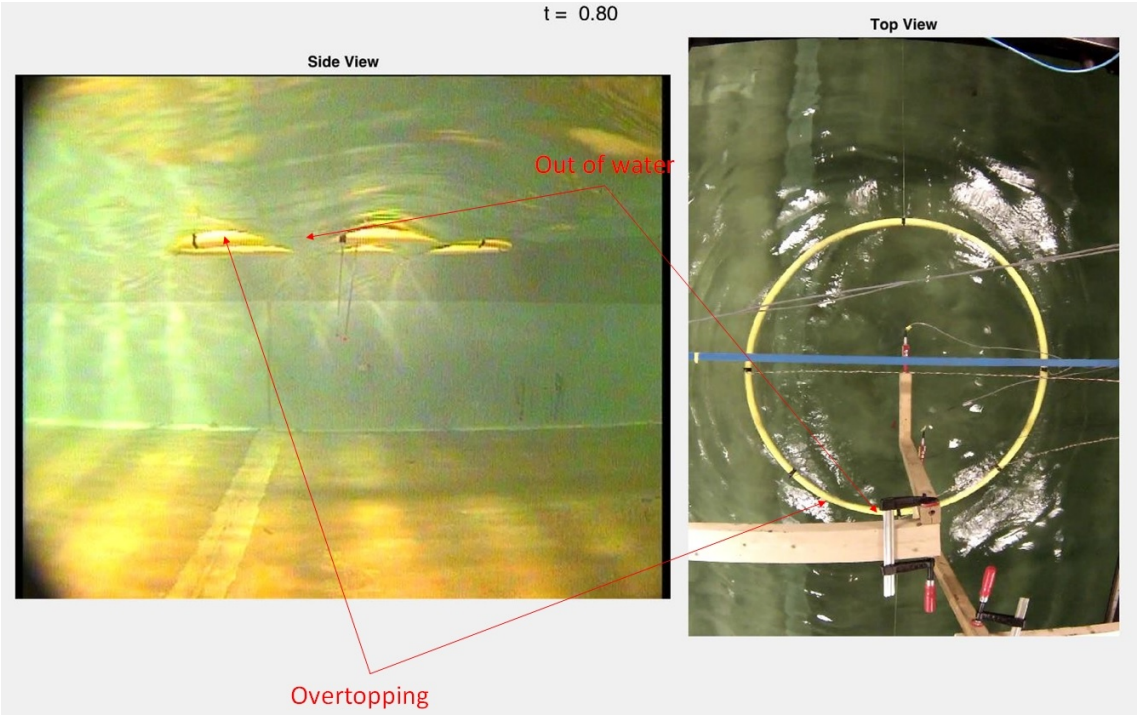

Figure 5: Illustrations of overtopping and out of water of parts of the torus in model tests (see also movie). Left: Side view from underwater camera; Right: Top view from the camera in air.

3. Theoretical methods

Ideally, we need a fully nonlinear 3D CFD method that accounts for hydroelasticity to compare with the experiments. We say 3D because the linear hydroelastic calculations of vertical accelerations of a torus in regular waves by Li and Faltinsen (2012) showed significant 3D hydrodynamic effects. We say fully nonlinear because the experiments show that even fourth order harmonics of the measured floater accelerations mattered in steeper waves and that perturbation methods are only practical for linear (first-order) and second-order problems, which determine only the first and second-harmonics as well as a constant of the floater acceleration in regular waves. Furthermore, Navier-Stokes equation is needed because flow separation may matter for steeper waves. Kristiansen and Faltinsen (2009) demonstrated the latter fact by 2D fully nonlinear CFD simulations of a semi-submerged circular floater in regular waves of relevance for fish farms. Laminar flow was assumed, which is appropriate in model test conditions at least for the boundary layer flow. The numerical method combined the Finite Difference Method and Chorin's projection method with the Constrained Interpolation Profile (CIP) method in the advection step. Furthermore, color functions were applied to capture the free surface. The numerical calculations agreed well with the presented experimental results. The fully nonlinear 3D CFD method for our case will need very long CPU time with state-of-the-art computational resources. Our choice was to investigate to what degree we can use state-of-the-art potential flow codes used in

engineering calculations.

Both the numerical methods used are based on potential flow theory for incompressible liquid and a perturbation scheme with the wave steepness as a small parameter, which is most relevant for the smallest experimental wave steepness. Surface tension is not included. Surface tension may affect the contact line between water and the floater. However, the difference appears as a thin layer of water rising up, but it does not affect the loading. In order for surface tension to matter, the wave length should be of the order of $1cm$ and smaller. These dimensions are clearly out of the range for incident waves and important nonlinear waves generated by the floater. One solver is HydroStar, which is a low-order Boundary Element Method solving the linear and second-order frequency-domain potential-flow problem in bichromatic incident waves in a consistent way. Deep-water conditions with monochromatic waves were assumed. The effect of mooring lines was included in the linear problem, but proved to be small. The commercial version of HydroStar accounts for tank wall interference in the linear problem but does not account for hydroelasticity, which matters in the experiments. The numerical results without tank wall interference were verified by convergence studies and we ensured that, the wave excitation force and moment by Haskind relationship and direct pressure integration agreed. Newman (1962) relationship between excitation force and moment amplitudes and corresponding wave radiation damping for an axisymmetric vertical body was satisfied. The second used solver is WAMIT which uses a higher-order Boundary Element Method. WAMIT provides linear generalized forces due to elastic vibration modes. It was combined with the following curved beam equation

$$m\frac{\partial^2 w}{\partial t^2} + \rho g b_w w + EI\frac{\partial^4 w}{\partial s^4} + \frac{EI}{c^2}\frac{\partial^2 w}{\partial s^2} = f_3(s)^{\text{added mass}+\text{damping}} + f_3(s)^{\text{wave excit}} \quad (1)$$

to describe the vertical motion w of the floater by using a modal approach. Here the differentiation $\partial/\partial s$ is along the torus, t is the time variable, m is the floater mass per unit length and EI is the bending stiffness. The bending stiffness term $\frac{EI}{c^2}\frac{\partial^2 w}{\partial s^2}$ is due to curvature effect of the torus (Love (2013)). Together with $EI\frac{\partial^4 w}{\partial s^4}$ it describes a rigid floater when $EI \to \infty$ and was erroneously not included by Li and Faltinsen (2012). $f_3^{\text{added mass}+\text{damping}}$ is the vertical added mass and damping force per unit length of the floater and $f_3^{\text{wave excit}}$ is the vertical wave excitation force on the floater per unit length of the floater. Both the hydrodynamic terms depend on the longitudinal coordinate 's' along the floater as denoted in Equation 1. Li and Faltinsen (2012) explicitly derived these 2D hydrodynamic terms by accounting for 3D flow. The term $\rho g b_w w$ is caused by the change of the buoyancy force due to the motion w. Here ρ is the mass density of water and b_w is $2a$. The hydroelastic model neglects mooring forces and coupling with longitudinal motions. Separate numerical studies with a rigid model showed small effects of mooring loads and coupling between surge and pitch. We do not know the structural damping, which is of concern for the resonance oscillations of elastic modes in case of small hydrodynamic damping. However, the numerical studies by Li et al. (2014) for a similar problem as ours indicate that structural damping

within realistic limits have a small effect.

We assume regular deep-water waves propagating along the positive x-axis. The vertical motion of the floater is expressed as the following Fourier series:

$$w \;=\; a_0\,(t) \;+\; \sum_{n=1}^{\infty} a_n\,(t)\cos n\beta \tag{2}$$

Here the angle β is defined in Figure 2. The x- and y- coordinates of the torus axis is given by $x = c\cos\beta$, $y = c\sin\beta$ where c is the torus radius. a_0 and $a_1\cos\beta$ describe heave at the torus axis and pitch, respectively. The other terms in Equation 2 are elastic modes. The two-dimensional added mass $a_{33}^{(n)}$ and damping coefficient $b_{33}^{(n)}$ due to vertical motion $a_n\cos n\beta$ gives the following vertical force per unit length:

$$f_3^{\text{added mass}+\text{damping}} \;=\; -a_{33}^{(n)}\ddot{a}_n\cos n\beta \;-\; b_{33}^{(n)}\dot{a}_n\cos n\beta \tag{3}$$

We substitute w given by Equation 2 into Equation 1. The resulting equation are then multiplied successively by $\cos n\beta, n = 0, 1, ..$ and integrated from $\beta = 0$ to 2π. The resulting generalized added mass, damping and wave excitation loads are calculated by WAMIT.

Due to the different theoretical features of the solvers, 4 different numerical models are used in the following studies and are listed in Table 2.

	Rigid	Elastic	Tank wall	Linear	Second order
HydroStar (model A)	YES	NO	NO	YES	NO
HydroStar (model B)	YES	NO	YES	YES	NO
HydroStar (model C)	YES	NO	NO	NO	YES
WAMIT (model D)	NO	YES	NO	YES	NO

Table 2: Numerical models used in this paper to consider a rigid or an elastic torus, tank wall interference, linear and second order hydrodynamic effects.

4. Experimental and numerical results

The numerical (model A) and experimental longitudinal motions and vertical accelerations were compared for the smallest tested wave height-to-wave length ratio $H/\lambda = 1/120$ when we can expect that a perturbation method is most appropriate.

4.1. Linear frequency-domain horizontal torus motion

Figure 6 presents comparisons between experimental measurements and linear numerical (model A) predictions of longitudinal motion response-amplitude-operators (RAO). The fact that experimental $RAOs$ obtained by measuring the mooring lines forces in front and aft differ means that hydroelasticity matter, but without being so clear as we will see for the vertical accelerations in the next section. Hydroelasticity effects were also observed in the

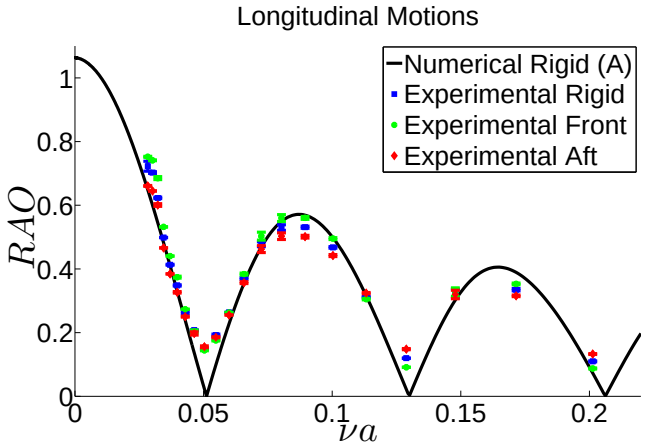

Figure 6: Theoretical and experimental linear frequency-domain results of longitudinal motions versus non-dimensional wave number νa. $RAO =$ longitudinal motion amplitude divided by prescribed incident wave amplitude ζ_a. The height of the experimental error bars is two times the estimated standard deviation. The wave height-to-wave length ratio $H/\lambda = 1/120$.

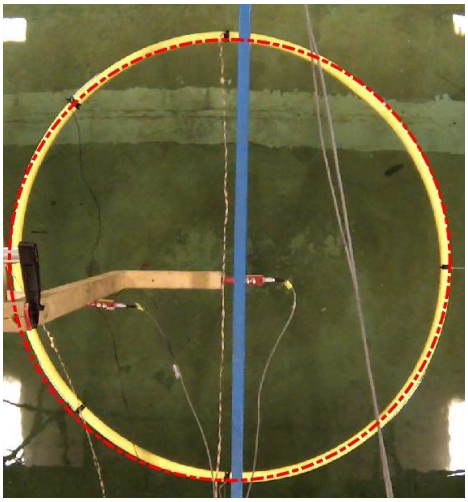

Figure 7: Floater deformation in calm conditions. Red line: prescribed torus; yellow colour: actual torus.

forces of the two transverse mooring lines along with small transverse rigid-body motions. An error source is that the presented torus is slightly deformed (see Figure 7). A satisfactory agreement between theory and experiments is shown in Figure 6. However, the theoretical cancellation effect at certain frequencies is not so pronounced in the experiments as in the numerical calculations. Figure 8 shows the experimental values for transverse motions. The frequency of the peak at $\nu a = 0.1132$ is close to the natural frequency of a transverse sloshing mode of the tank with a node at the centre plane of the tank. Since roll and transverse motions are coupled, the results in Figure 8 imply non-zero roll.

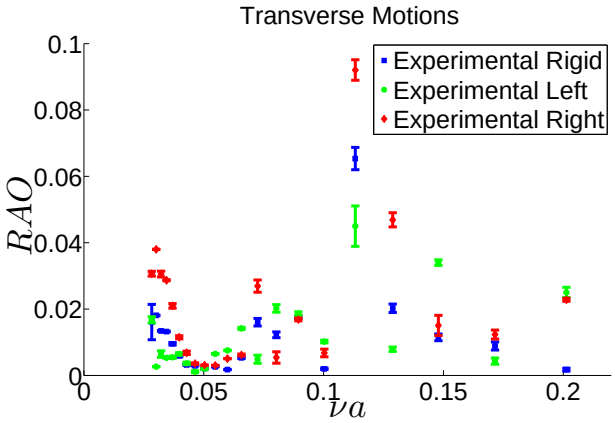

Figure 8: Experimental linear frequency-domain results of transverse motions versus non-dimensional wave number νa. RAO = transverse motion amplitude divided by prescribed incident wave amplitude ζ_a. The height of the experimental error bars is two times the estimated standard deviation. The wave height-to-wave length ratio $H/\lambda = 1/120$. Right is defined along positive y-axis in Figure 2.

4.2. Linear frequency-domain vertical torus accelerations

Figure 9 shows the numerical predictions of the non-dimensional linear frequency-domain vertical acceleration amplitude along five positions of the floater. Linear numerical results from HydroStar (with and without tank wall interference, *i.e.* model B and A, respectively, see Table 2) and WAMIT (with hydroelastic model, *i.e.* model D in Table 2) are reported as a function of the non-dimensional wave number νa, and compared with the corresponding experimental data. The experimental results are given with an error bar whose height is two times the standard deviation, which expresses that the oscillations are not steady state. The reason why the experimental results are not steady state can be wave reflections from the wave beach and the wave maker, build-up of transverse sloshing due to tank wall interference as well as beating effects induced by residual waves from the previous run with different period. The elastic modes $\cos 2\beta$, $\cos 3\beta$ and $\cos 4\beta$ influence the numerical hydroelastic results with the $\cos 2\beta$-mode giving the dominant contribution. The latter mode does not contribute at the front left and aft left positions with the consequence that the rigid and elastic results are closest there. Bending stiffness matters and causes the theoretical results coming closer to the experiments except at front left position. The peaks in the numerical results with tank wall interference (model B) correspond to the natural frequencies $\nu a = 0.0349, 0.0526, 0.0701, 0.0877, 0.1052, 0.1227, 0.1403, 0.1578, 0.1753, 0.1929$ associated with 2D transverse sloshing modes that are symmetric with respect to the longitudinal center-plane of the tank. The fact that the response is not infinite at the resonance frequencies as a 2D linear frequency domain theory predicts is a consequence of 3D flow. However, the calculations with tank wall interference do not improve the agreement between theory and experiments. For instance, the experimental results at $\nu a = 0.1715$, which is close to the 2D natural sloshing frequency $\nu a = 0.1753$, do not seem to be influenced by the clear theoretical resonance demonstrated for the rigid torus. However, the experi-

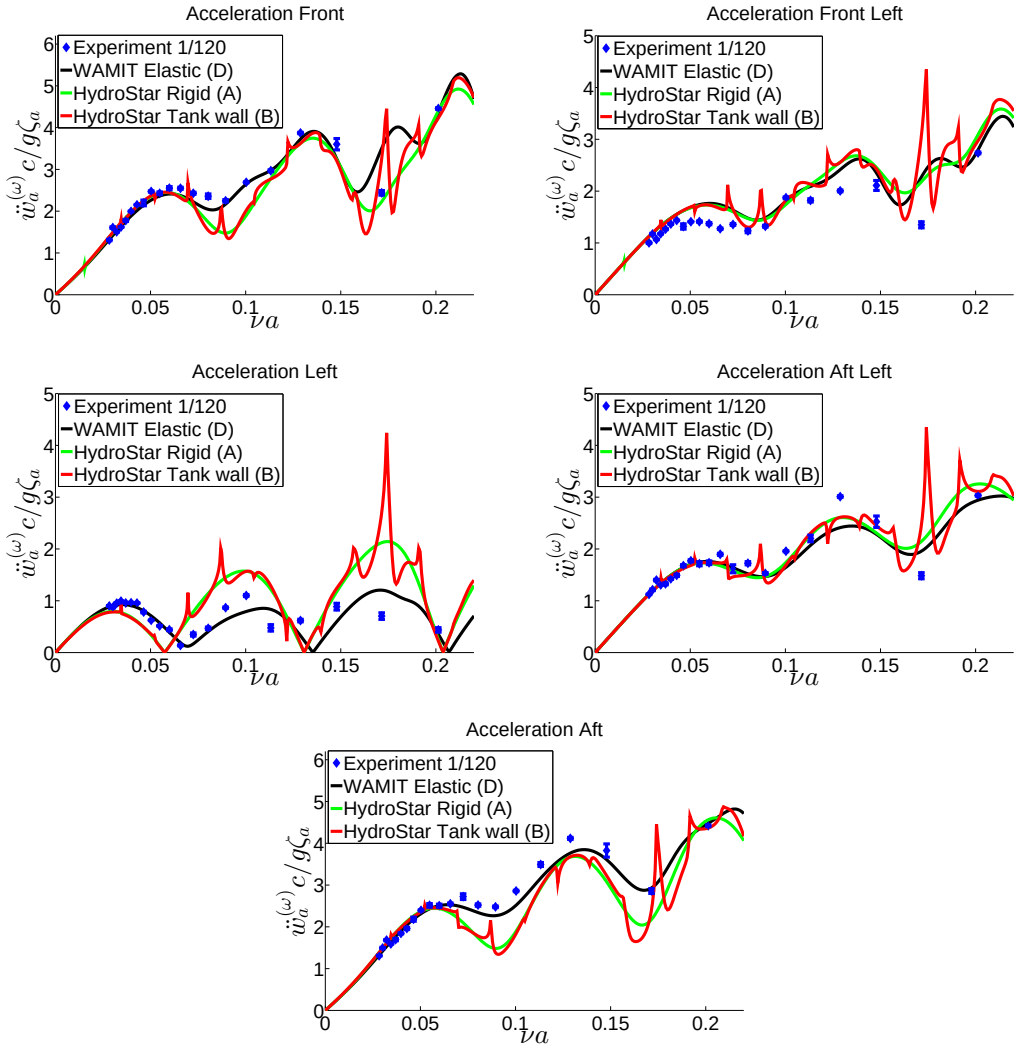

Figure 9: Comparison of linear frequency-domain results of vertical acceleration amplitude $\ddot{w}_a^{(\omega)}$ along the floater by means of HydroStar and WAMIT with experiments versus non-dimensional wave number νa. WAMIT results are combined with hydroelastic curved-beam theory. The height of the experimental error bars is two times the estimated standard deviation. The wave height-to-wave length ratio $H/\lambda = 1/120$.

mental time-domain results show a beating effect associated with the difference frequency between the forcing frequency and the sloshing frequency $\nu a = 0.1715$, which indicates that a build-up of resonance occurs.

Amplitudes $\ddot{a}_{na}$ and phase angles α_n of the different acceleration modes defined by $\ddot{a}_n = \ddot{a}_{na} \cos(\omega t + \alpha_n)$ with the incident wave elevation given by $\zeta = \zeta_a \sin(\omega t - \nu x)$ were experimentally and theoretically (model D) identified. Experimentally we determined amplitudes and phases for $n = 0, 1, 2, 3, 4$ by satisfying:

$$\ddot{w} \;=\; \ddot{a}_0\,(t) \;+\; \ddot{a}_1\,(t)\cos\beta \;+\; \ddot{a}_2\,(t)\cos 2\beta \;+\; \ddot{a}_3\,(t)\cos 3\beta \;+\; \ddot{a}_4\,(t)\cos 4\beta \tag{4}$$

at the five measurement points. The procedure was to consider the time instant when the experimental vertical acceleration at the front point had a maximum value close to the experimental mean amplitude. In more details, it means that we first expressed the experimental values of the different acceleration modes as $\ddot{a}_{na}\cos(\omega t' + \gamma_n)$ with $t' = 0$ corresponding to when the front vertical acceleration had the considered maximum. By selecting also the time instant $\omega t' = \pi/2$ we have sufficient equations to determine the amplitudes $\ddot{a}_{na}$ and the phase angles γ_n. Sensitivity to selecting different time instants was small. Since we did not measure the incident waves, we used the theoretical values of the vertical acceleration at the front point as a reference to determine the experimental phases relative to the theoretical incident wave elevation. It means that we write $t = t' - \delta$ in the theoretical vertical acceleration at the front point with five modes, *i.e.*

$$\begin{aligned}
\ddot{w}|_{\beta=0} \;&=\; \left(\sum_{n=0}^{4}\ddot{a}_{na}\cos\alpha_n\right)\cos(\omega t' - \omega\delta) \;-\; \left(\sum_{n=0}^{4}\ddot{a}_{na}\sin\alpha_n\right)\sin(\omega t' - \omega\delta) \\
&=\; \left[\left(\sum_{n=0}^{4}\ddot{a}_{na}\cos\alpha_n\right)\cos\omega\delta \;+\; \left(\sum_{n=0}^{4}\ddot{a}_{na}\sin\alpha_n\right)\sin\omega\delta\right]\cos\omega t' \\
&+\; \left[\left(\sum_{n=0}^{4}\ddot{a}_{na}\cos\alpha_n\right)\sin\omega\delta \;-\; \left(\sum_{n=0}^{4}\ddot{a}_{na}\sin\alpha_n\right)\cos\omega\delta\right]\sin\omega t'
\end{aligned} \tag{5}$$

By requiring the theoretical vertical acceleration at the front point to behave as $A\cos\omega t'$, $A > 0$ we get the following requirements:

$$\begin{aligned}
&\left(\sum_{n=0}^{4}\ddot{a}_{na}\cos\alpha_n\right)\sin\omega\delta \;-\; \left(\sum_{n=0}^{4}\ddot{a}_{na}\sin\alpha_n\right)\cos\omega\delta \;=\; 0 \\
&\left(\sum_{n=0}^{4}\ddot{a}_{na}\cos\alpha_n\right)\cos\omega\delta \;+\; \left(\sum_{n=0}^{4}\ddot{a}_{na}\sin\alpha_n\right)\sin\omega\delta \;>\; 0
\end{aligned} \tag{6}$$

This determines δ. By substituting $t' = t + \delta$ into $\ddot{a}_{na}\cos(\omega t' + \gamma_n)$ we determine experimental phase angles α_n. The comparison between theory (model D) and experiments are presented in Figure 10 and Figure 11 for $n = 0, 1, 2$, *i.e.* for heave, pitch and the lowest elastic mode. The amplitudes for $n = 3, 4$ are small relative to the values for $n = 0, 1, 2$ and are therefore not shown. The fact that the heave motion should follow the incident wave elevation at $x = 0$ and pitch with a positive value in an $Oxyz$ coordinate system as defined in Faltinsen (1990) should be 180° out of phase with the incident wave slope at $x = 0$ when $\nu a \to 0$ is confirmed. General good agreement is obtained, in particular for pitch acceleration amplitudes. Differences between theoretical (model D) and experimental accelerations of heave and lowest elastic mode amplitude are noted for $\nu a = 0.1715$ and are the reasons for the differences noted at this frequency in Figure 9. The difference is largest for heave

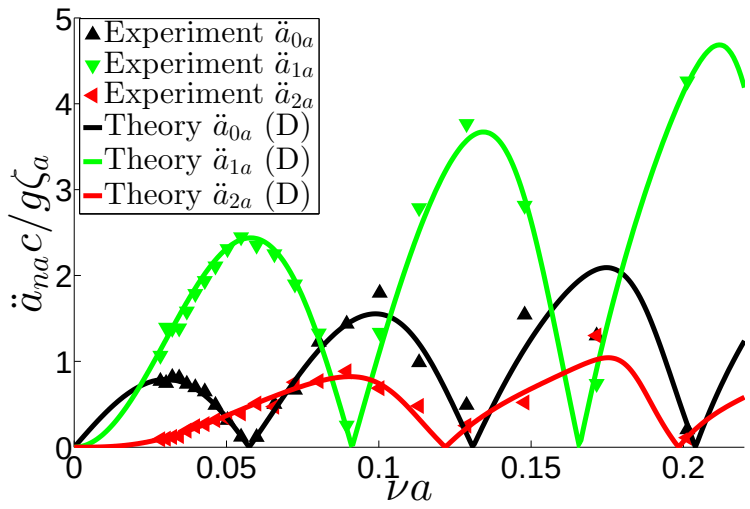

Figure 10: Comparison of experimental and theoretical linear frequency-domain results of vertical acceleration amplitudes $\ddot{a}_{na}$ of heave ($n = 0$), pitch ($n = 1$) and lowest elastic mode ($n = 2$) versus non-dimensional wave number νa. The wave height-to-wave length ratio $H/\lambda = 1/120$.

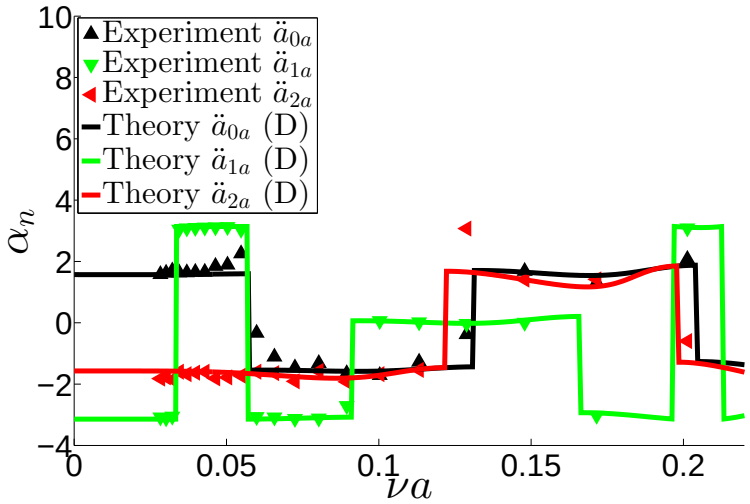

Figure 11: Comparison of experimental and theoretical linear frequency-domain results of vertical acceleration phase angles α_n of heave ($n = 0$), pitch ($n = 1$) and lowest elastic mode ($n = 2$) versus non-dimensional wave number νa. The wave height-to-wave length ratio $H/\lambda = 1/120$.

accelerations.

We investigated in more detail possible tank-wall interference effects by analyzing the wave amplitude due to torus motions at the tank walls along a wave-propagation direction perpendicular to the tank walls by using theory without tank wall effects. The analysis

is done by relating the far-field wave amplitudes due to forced oscillations of the different modes to the generalized damping coefficients for the different modes by using conservation of kinetic and potential energy in the water.

The far-field expression of the velocity potential for a given mode can be obtained by a line distribution of sources along the centerline of the torus (Li and Faltinsen (2012)). A frequency-domain analysis in infinite water depth and infinite horizontal water extent was considered. The sources satisfy the classical linearized free-surface condition and radiation condition. The far-field waves are expressed in terms of Hankel functions. The analysis by Li and Faltinsen (2012) shows that the source density associated with mode n varies as $\cos n\beta$. It follows by combining the latter fact with properties of Bessel functions that the far-field velocity potential associated with mode n can be approximated as:

$$\varphi_n = \frac{g}{\omega}\frac{A_n \cos n\theta}{\sqrt{\nu r}} exp\left(\nu z\right)\cos\left(\omega t - \nu r + \delta_n\right) \tag{7}$$

Here (r, θ, z) are polar coordinates with the angle θ having the same definition as the angle β in Figure 2. Energy considerations based on a general formula within potential flow of an incompressible liquid (see, for instance, Newman (1977)) imply that:

$$\frac{dE}{dt} = \int_{S_B}\left(p - p_a\right)U_n ds \; - \; \rho\int_{S_\infty}\frac{\partial\varphi_n}{\partial t}\frac{\partial\varphi_n}{\partial n}ds \tag{8}$$

Here S_B is the mean wetted body surface and S_∞ is a vertical circular cylindrical control surface at large $r = R$ extending from $z = 0$ to $z = -\infty$. E is the sum of the kinetic and potential energy in the water domain Ω between S_B and S_∞. The positive direction of the normal coordinate n is into the water domain Ω. p is the pressure with subscript a indicating atmospheric pressure. U_n means the normal velocity of S_B. We integrate Equation 8 over the oscillation period T with the consequence that the term on the left hand side does not contribute due to periodicity of E. The first term on the right hand side leads to

$$\omega^2\frac{T}{2}B_{33}^{(n)}a_{na}^2, \quad B_{33}^{(n)} = \int_0^{2\pi} b_{33}^{(n)}\cos^2 n\beta c d\beta \tag{9}$$

The second term on the right hand side is

$$-\frac{\rho g^2 A_n^2}{\omega 2\nu}\frac{T}{2}I_n \tag{10}$$

where $I_0 = 2\pi, I_n = \pi$ when $n = 1, 2, ...$ This means

$$\left(\frac{A_n}{a_{na}}\right)^2 = \frac{2B_{33}^{(n)}\nu^3}{\rho\omega I_n} \tag{11}$$

We consider now the wave propagation direction perpendicular to the tank wall, *i.e.* $\theta = \pm\pi/2$. Equation 7 shows no contribution from pitch at $\theta = \pm\pi/2$. The effect of heave and the lowest elastic mode will be considered. The corresponding wave amplitudes at the tank walls normalized by the incident wave amplitude can be expressed as:

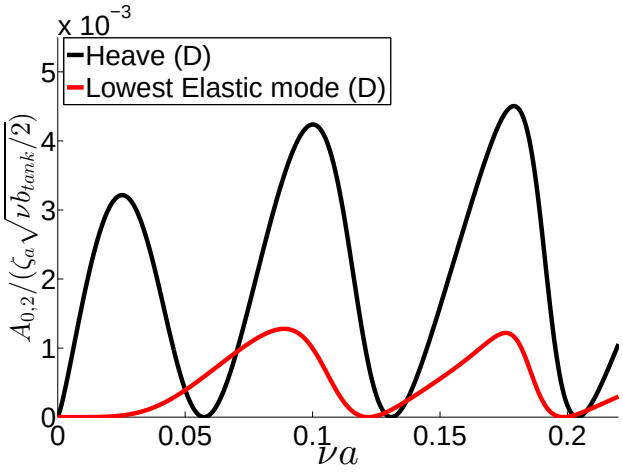

Figure 12: Wave amplitude at the tank walls along a wave-propagation direction perpendicular to the tank due to torus motions in heave and lowest elastic mode (model D) normalized by incident wave amplitude walls versus non-dimensional wave number νa. Note that the effect of the tank wall is not included in model D.

$$\frac{A_n}{\zeta_a\sqrt{\nu b_{tank}/2}} = 2\nu\frac{a_{na}}{\zeta_a}\sqrt{\frac{B_{33}^{(n)}}{\rho\omega I_n b_{tank}}} \tag{12}$$

Here b_{tank} is the tank breadth. The results are shown in Figure 12 and should be interpreted as an excitation of tank wall interference. The amplitudes are small relative to the incident wave amplitude and show a strong frequency dependency with zeroes and peaks. For instance, there is a peak at $\nu a = 0.1792$, which is close to the 2D sloshing frequency $\nu a = 0.1753$.

Even though the agreement between linear theory (model A, B and D) and experiments presented in Figure 9, Figure 10 and Figure 11 is generally satisfactory we investigated error sources. It has already been mentioned that coupling between longitudinal and vertical motions is present and is neglected in the hydroelastic analysis. Another error source is that the measured incident wave amplitude differed from the intended wave amplitude as illustrated in Figure 4. Since small-amplitude sway occurred in the experiments, small-amplitude roll must be present due to coupling and cause a vertical motion.

Viscous effects matter when significant viscous flow separation occurs. A measure of flow separation for ambient oscillatory planar 2D flow with flow velocity amplitude U_a and period T past a stationary circular cylinder of diameter $2a$ in infinite fluid is the Keulegan-Carpenter number $KC = U_a T/(2a)$. When $KC < 2-3$, flow separation does not occur (Faltinsen (1990)). We can generalize these findings to our case with a rigid torus and define the vertical and radial Keulegan-Carpenter numbers $KC_{vert.} = \pi\eta_{rel.ver.}/a$ and $KC_{rad.} = u_{rel.rad.}T/(2a)$. Here $\eta_{rel.vert.}$ is the amplitude of the relative vertical motion between the floater and the incident waves. $u_{rel.rad.}$ means the amplitude of the relative velocity component in the radial direction between the floater and the incident waves. Since the torus follows the waves when

$\nu a \to 0$, $\eta_{rel.vert.}/\zeta_a$ and $u_{rel.rad.}T/\zeta_a$ go to zero when $\nu a \to 0$. Calculated values of $KC_{vert.}$ and $KC_{rad.}$ by HydroStar (model A) are presented in Figure 13 versus the non-dimensional wave number for five positions along the floater. Because the wave height for a given wave steepness goes to infinity when $\nu a \to 0$, $KC_{rad.}$ does not tend to zero when $\nu a \to 0$. The results indicate that flow separation is insignificant for our considered small wave steepness and that we have an attached boundary layer flow.

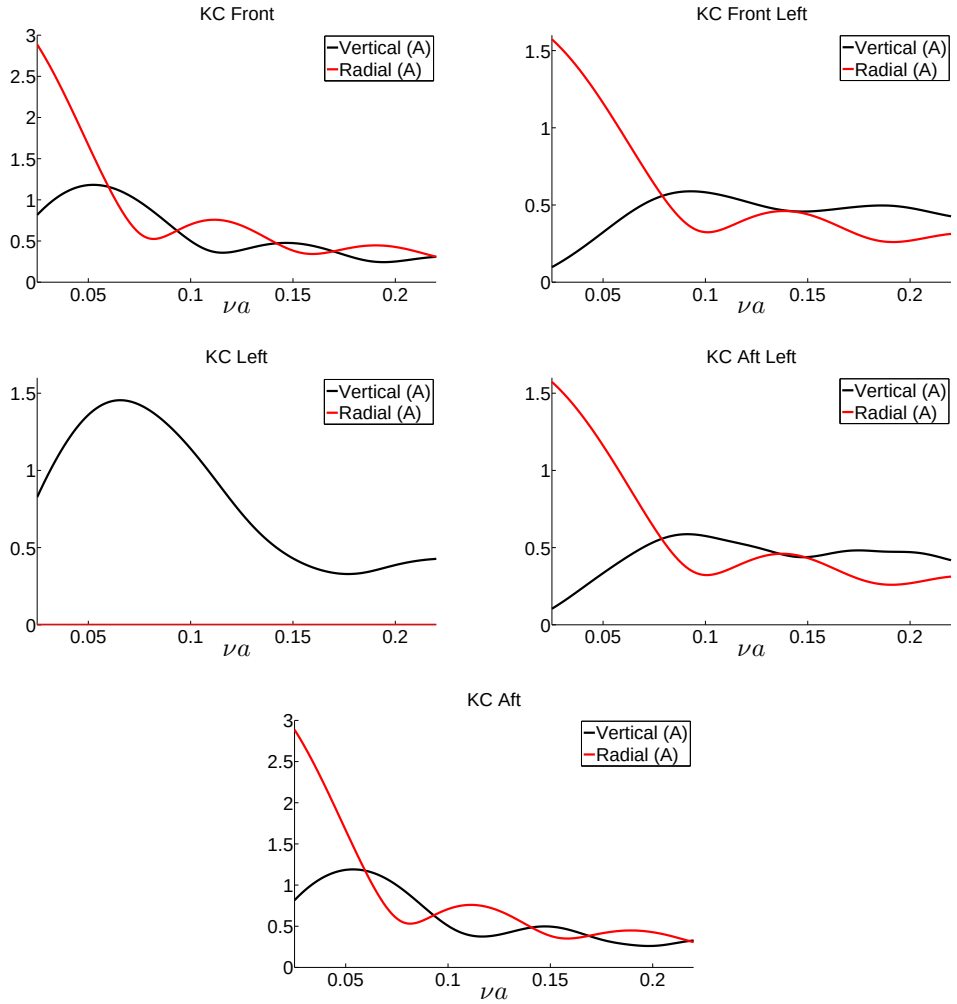

Figure 13: Calculated vertical and radial Keulegan-Carpenter numbers versus non-dimensional wave number νa for five positions along the floater. The wave height-to-wave length ratio $H/\lambda = 1/120$.

The attached viscous boundary-layer flow along the torus has been analyzed by assuming laminar boundary-layer flow and ambient longitudinal flow velocity $U_a \cos \omega t$ together with a rigid free-surface condition. The latter fact avoids the necessity to consider all the details of the frequency-dependent pressure distribution. The torus is assumed semi-submerged. We apply the cross-flow principle together with strip theory and well-established 2D results

based on Stokes second problem (Faltinsen (1990)), which gives:

$$F_1^{visc} = U_a \sqrt{\frac{\omega\mu}{\rho}} \cos(\omega t + \pi/4)\, 2ac\pi^2 \tag{13}$$

as the longitudinal viscous force on the semi-submerged torus. Here μ is the dynamic viscosity coefficient. We consider the viscous force in phase with the acceleration and compare it with the measure $\rho\pi^2 a^2 2c\omega U_a \sin\omega t$ of the sum of the mass and added mass acceleration force on the torus. Here we have not accounted for the fact that the added mass in surge is frequency dependent. The ratio of the viscous force amplitude and the measure of the mass and added mass force can be expressed as:

$$\frac{F_v}{F_{mass}} = \sqrt{\frac{\mu}{2\omega\rho a^2}} \tag{14}$$

The results are presented in Figure 14 as a function of νa in our considered frequency range. Since the maximum value of $\frac{F_v}{F_{mass}}$ is about 0.02, we confirm that viscous effects are not dominant.

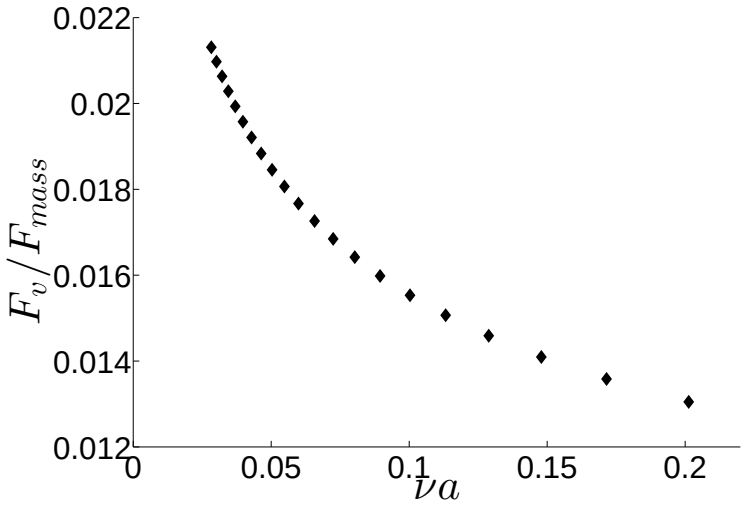

Figure 14: The ratio F_v/F_{mass} of the amplitudes of viscous force in phase with surge acceleration and a measure of the mass and added mass force in surge on the torus as a function of non-dimensional wave number νa.

Nonlinear effects may cause oscillations with frequency ω. For instance, if we apply a third-order theory with steady-state oscillations in regular waves, there are oscillations with frequencies ω and 3ω. The corresponding amplitudes are expected to be of the same order of magnitude. Our arguments for saying this is that a third-order analysis, for instance involves terms $\cos^3\omega t = \frac{1}{4}\cos 3\omega t + \frac{3}{4}\cos\omega t$. Therefore, we present in Figure 15 the experimental ratio $\ddot{w}_a^{(3\omega)}/\ddot{w}_a^{(\omega)}$ versus non-dimensional wave number νa for the five considered positions

along the floater. Here $\ddot{w}_a^{(3\omega)}$ and $\ddot{w}_a^{(\omega)}$ are the vertical acceleration amplitudes of the oscillations with frequencies 3ω and ω, respectively. The mean values obtained from the DFT analysis are the basis for the estimates, *i.e.* we do not involve an error band associated with the standard deviation. The results indicate that third order effects cannot be neglected in estimating the experimental accelerations oscillating with frequency ω for $\nu a \lessapprox 0.1$. One contributing factor to the larger relative influence for small νa is that the incident wave amplitude-to-cross-sectional radius ratio $\zeta_a/a = (\pi/120)/\nu a$ increases with decreasing νa.

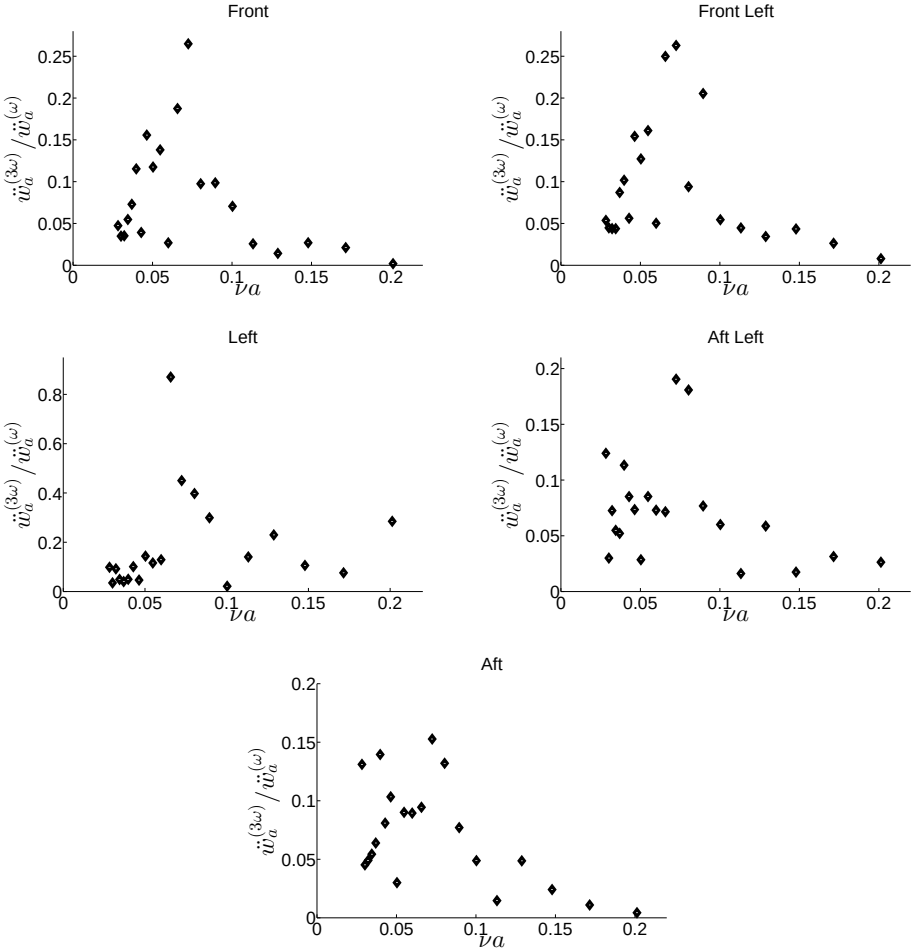

Figure 15: Experimental ratio $\ddot{w}_a^{(3\omega)}/\ddot{w}_a^{(\omega)}$ versus non-dimensional wave number νa for five positions along the floater. Here $\ddot{w}_a^{(3\omega)}$ and $\ddot{w}_a^{(\omega)}$ are the vertical acceleration amplitudes of the oscillations with frequencies 3ω and ω, respectively. The wave height-to-wave length ratio $H/\lambda = 1/120$.

4.3. Sum-frequency vertical torus accelerations

Since the measurements are relative to a body-fixed coordinate system $O\overline{xyz}$, which coincides with the $Oxyz$-system at rest and the calculations by HydroStar (model C) are in

an inertial coordinate system, we have to add the sum-frequency part of $\ddot{\eta}_1\eta_5 + \frac{1}{2}g\eta_5^2$ to the sum-frequency calculations of vertical accelerations. Here $\ddot{\eta}_1$ and η_5 are the surge acceleration and pitch angle, respectively. The influence of the correction term was negligible.

Figure 16 and Figure 17 show numerically predicted second-order sum-frequency non-dimensional acceleration amplitude $\ddot{w}_a^{(2\omega)}c^2/\left(g\zeta_a^2\right)$ along the $\overline{z}$-axis for five positions of the floater by HydroStar (model C) together with experimental results versus non-dimensional wave number νa. The large differences in vertical scale of the two figures should be noted. The agreement is not perfect but we should have in mind the error sources discussed in the section on linear frequency-domain results, which implicitly have consequences for the second-order solution. Additional tank-wall interference effects occur for the second-order problem since the second-order potential involves contributions from the non-homogenous free-surface conditions over an infinite domain of the mean free surface, which is in conflict with the tank walls. We documented for the linear problem the fact that there was in the experiments non-negligible oscillations with frequency 3ω meant that there were contributing oscillations with ω from a third-order theory. In theory, we may say that there are contributions with frequencies 2ω and 4ω from a fourth-order theory. However, since the measured 4ω-component was small, we anticipate that the corresponding 2ω-component can be neglected. The numerical results show clear peaks at the higher frequencies, but there are no experimental values at those peak frequencies. The peaks are associated with peaks in the excitation loads. There are no resonance effects caused by 2ω being equal to an undamped natural frequency.

4.4. Wave elevation inside floater

The wave elevation inside the floater was investigated experimentally and theoretically. The linear potential flow theory predicts, for instance, zero heave and pitch wave radiation damping at certain frequencies, which differ for heave and pitch. The latter fact suggests that wave resonances inside are possible. Figure 18 shows the results. Linear potential flow theory for the rigid torus without tank wall interference (model A) has been applied. The upper graph is for the centre of the inside of the floater. There is no evidence of resonance neither in experiments nor theory. However, since linear resonant waves would have a node at that point, we have numerically also studied the wave elevation at the front and aft of the inside of the floater versus non-dimensional wave number (see Figure 18). Still we do not see any clear evidence of resonance.

5. Experimental higher-harmonic torus accelerations in waves of different steepness

Figure 19 presents steady-state amplitudes of experimental non-dimensional harmonic acceleration $\ddot{w}_a^{(\omega)}$, second-harmonic acceleration $\ddot{w}_a^{(2\omega)}$, third-harmonic acceleration $\ddot{w}_a^{(3\omega)}$ and fourth-harmonic acceleration $\ddot{w}_a^{(4\omega)}$ along body-fixed $\overline{z}$-axis versus non-dimensional wave number νa for wave height-to-wavelength ratios $1/120, 1/60, 1/30$ and $1/15$ for floater front position ($\beta = \pi$) and left position ($\beta = \pi/2$) in incident regular waves with frequency ω

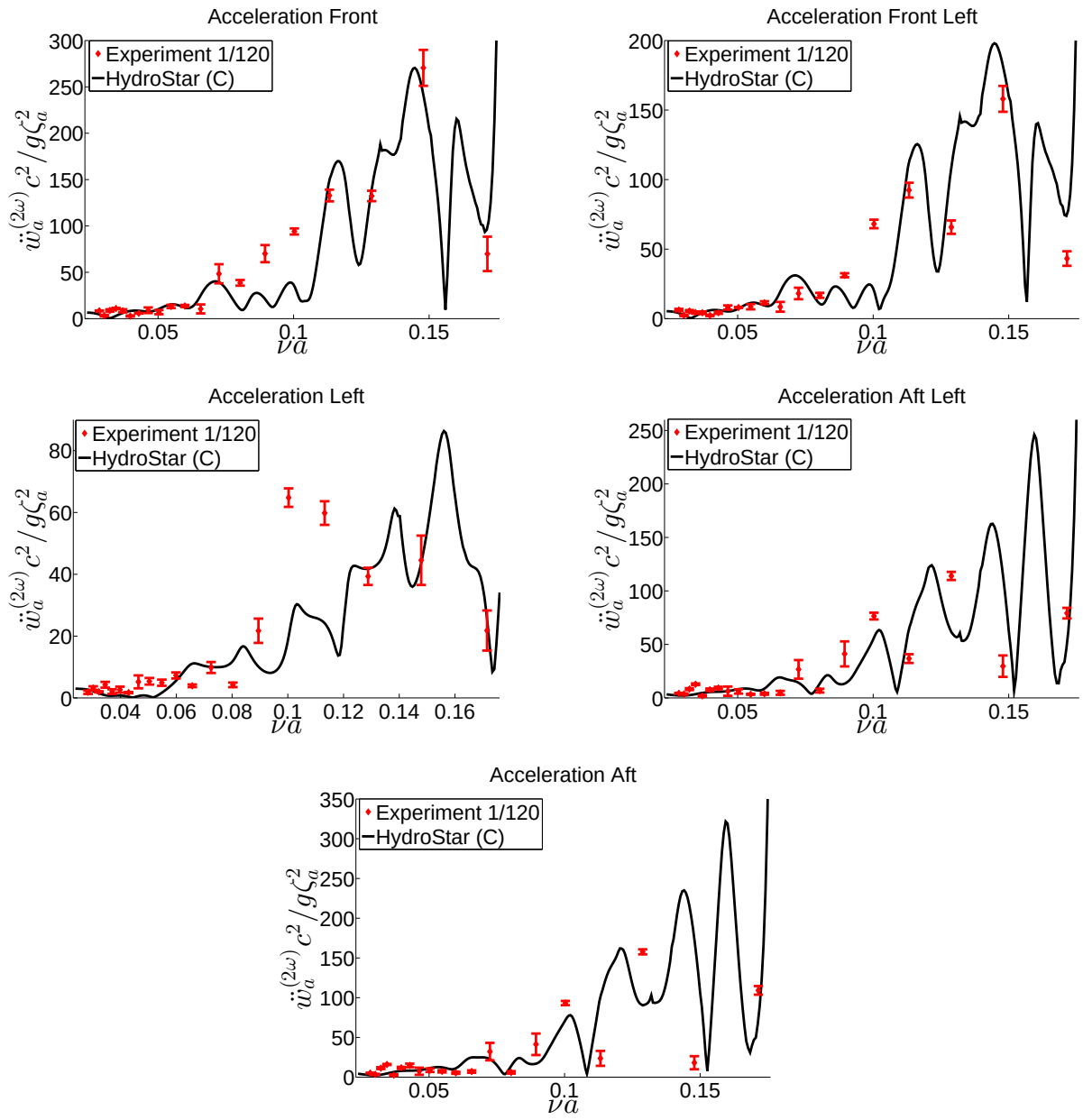

Figure 16: Second-order sum-frequency non-dimensional vertical acceleration amplitude $\ddot{w}_a^{(2\omega)} c^2 / (g\zeta_a^2)$ along the $\overline{z}$-axis for five positions of the floater by HydroStar (model C) together with experimental results versus non-dimensional wave number νa in the range of $[0.023, 0.176]$. The height of the experimental error bars is two times the estimated standard deviation. The wave height-to-wave length ratio $H/\lambda = 1/120$.

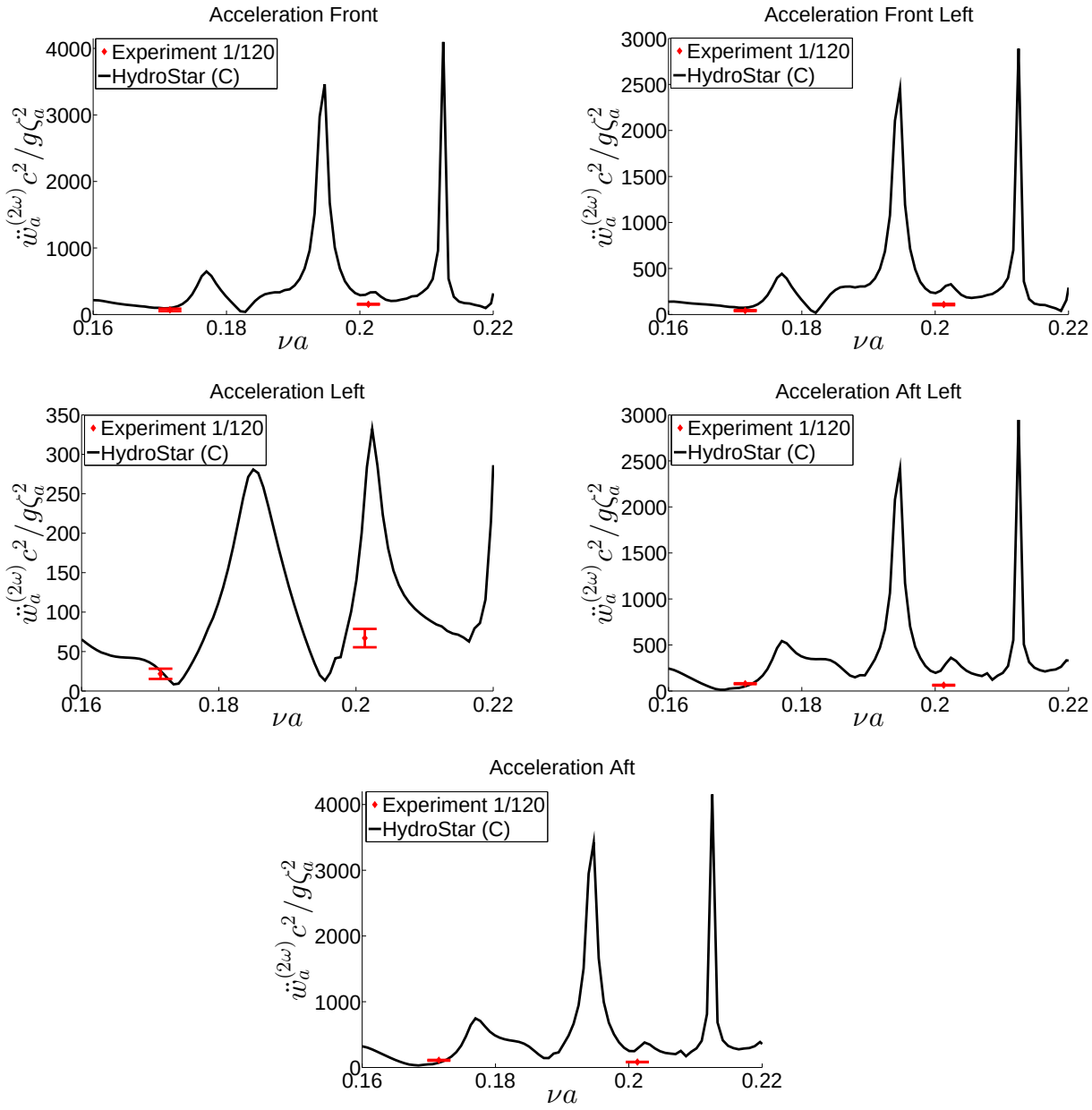

Figure 17: Second-order sum-frequency non-dimensional vertical acceleration amplitude $\ddot{w}_a^{(2\omega)} c^2 / (g\zeta_a^2)$ along the $\overline{z}$-axis for five positions of the floater by HydroStar (model C) together with experimental results versus non-dimensional wave number νa in the range of $[0.16, 0.22]$. The height of the experimental error bars is two times the estimated standard deviation. The wave height-to-wave length ratio $H/\lambda = 1/120$.

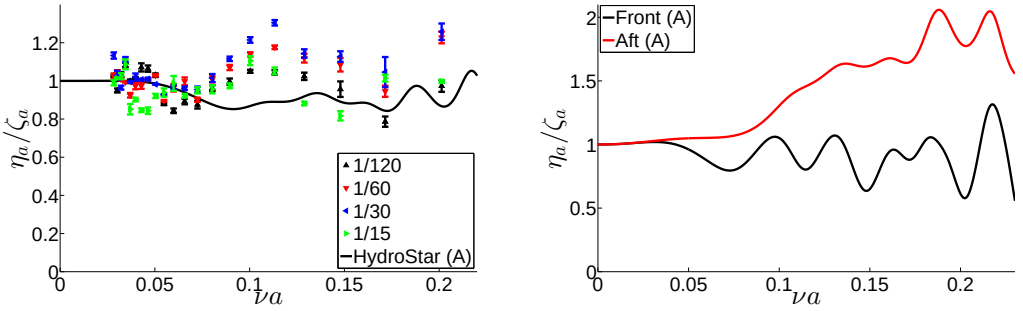

Figure 18: Left drawing: Measured and numerically predicted wave amplitude η_a in the centre of the inside of the floater. Right drawing: Numerically predicted wave amplitude in the front and aft of the inside of the floater. Linear potential flow theory for the rigid torus without tank wall interference (model A) is used. The height of the experimental error bars is two times the estimated standard deviation. Experiments are for wave height-to-wavelength ratios $1/120, 1/60, 1/30$ and $1/15$.

and amplitude ζ_a. We decided to make the harmonic terms non-dimensional in the same manner in order to compare the magnitudes of the different harmonic terms. The results show significant contributions from all the presented harmonic terms, in particular for higher wave height-to-wavelength ratios. The contributions from higher than fourth-order terms were not significant and are not presented.

Since $\ddot{w}_a^{(\omega)}$, $\ddot{w}_a^{(2\omega)}$, $\ddot{w}_a^{(3\omega)}$ and $\ddot{w}_a^{(4\omega)}$ are according to a perturbation method mainly proportional to respectively ζ_a, ζ_a^2, ζ_a^3 and ζ_a^4, we have presented in Figure 20 $\ddot{w}_a^{(2\omega)}/\zeta_a^2$, $\ddot{w}_a^{(3\omega)}/\zeta_a^3$, $\ddot{w}_a^{(4\omega)}/\zeta_a^4$ along body-fixed $\overline{z}$-axis versus wave number νa for different wave steepness for floater front position ($\beta = \pi$) and left position ($\beta = \pi/2$). We start by examining $\ddot{w}_a^{(\omega)}/\zeta_a$ in Figure 19, which shows that $\ddot{w}_a^{(\omega)}$ is mainly proportional to ζ_a for the different wave steepness $1/120, 1/60, 1/30$ and $1/15$. However, there ought to be a dependence on ζ_a^3 as earlier argued. When it comes to $\ddot{w}_a^{(2\omega)}/\zeta_a^2$ and we disregard the results for the highest wave steepness $1/15$, $\ddot{w}_a^{(2\omega)}$ is mainly proportional to ζ_a^2 for the wave steepness $1/120, 1/60$ and $1/30$ at the front of the floater (see Figure 20). However, there ought to be a dependence on ζ_a^4 as earlier argued. When it comes to $\ddot{w}_a^{(3\omega)}$ and $\ddot{w}_a^{(4\omega)}$, we cannot say that they are mainly proportional to ζ_a^3 and ζ_a^4, respectively. It means that we cannot explain the behavior of $\ddot{w}_a^{(3\omega)}$ and $\ddot{w}_a^{(4\omega)}$ by a perturbation method with the wave steepness as a small parameter. The torus shape above the mean free surface becomes a factor. Actually, ζ_a/a ought to be considered as a small parameter. However, wave overtopping was observed during the experiments (see Figure 5). An estimate of occurrence of wave overtopping can be made by means of the vertical Keulegan-Carpenter number $KC_{vert.} = \pi\eta_{rel.vert.}/a$ presented in Figure 13 for different frequencies and torus positions and wave steepness $H/\lambda = 1/120$. We consider as an example $\pi\eta_{rel.vert.}/a = 1.5$ from Figure 13, which means that wave overtopping occurs for $H/\lambda > 1.4/120$. However, the latter estimate does not account for nonlinearities and local free-surface effects at the torus. An attempt was made to follow a common engineering

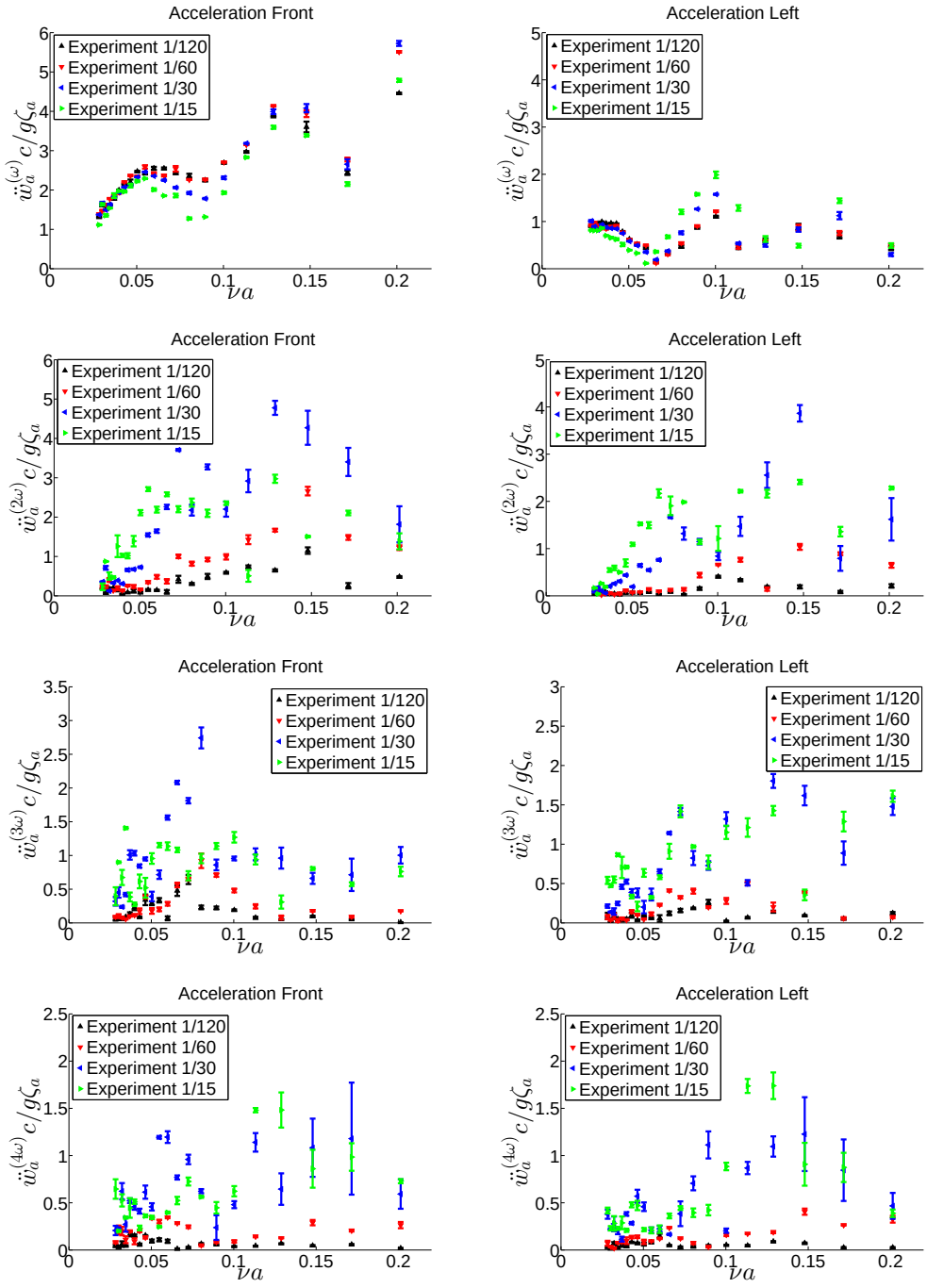

Figure 19: Steady-state amplitudes of experimental non-dimensional harmonic acceleration $\ddot{\bar{w}}_a^{(\omega)}$, second-harmonic acceleration $\ddot{\bar{w}}_a^{(2\omega)}$, third-harmonic acceleration $\ddot{\bar{w}}_a^{(3\omega)}$ and fourth-harmonic acceleration $\ddot{\bar{w}}_a^{(4\omega)}$ along body-fixed $\overline{z}$-axis versus non-dimensional wave number νa for wave height-to-wavelength ratios $1/120, 1/60, 1/30$ and $1/15$ for floater front position ($\beta = \pi$) and left position ($\beta = \pi/2$) in incident regular waves with frequency ω and amplitude ζ_a. The height of the experimental error bars is two times the estimated standard deviation.

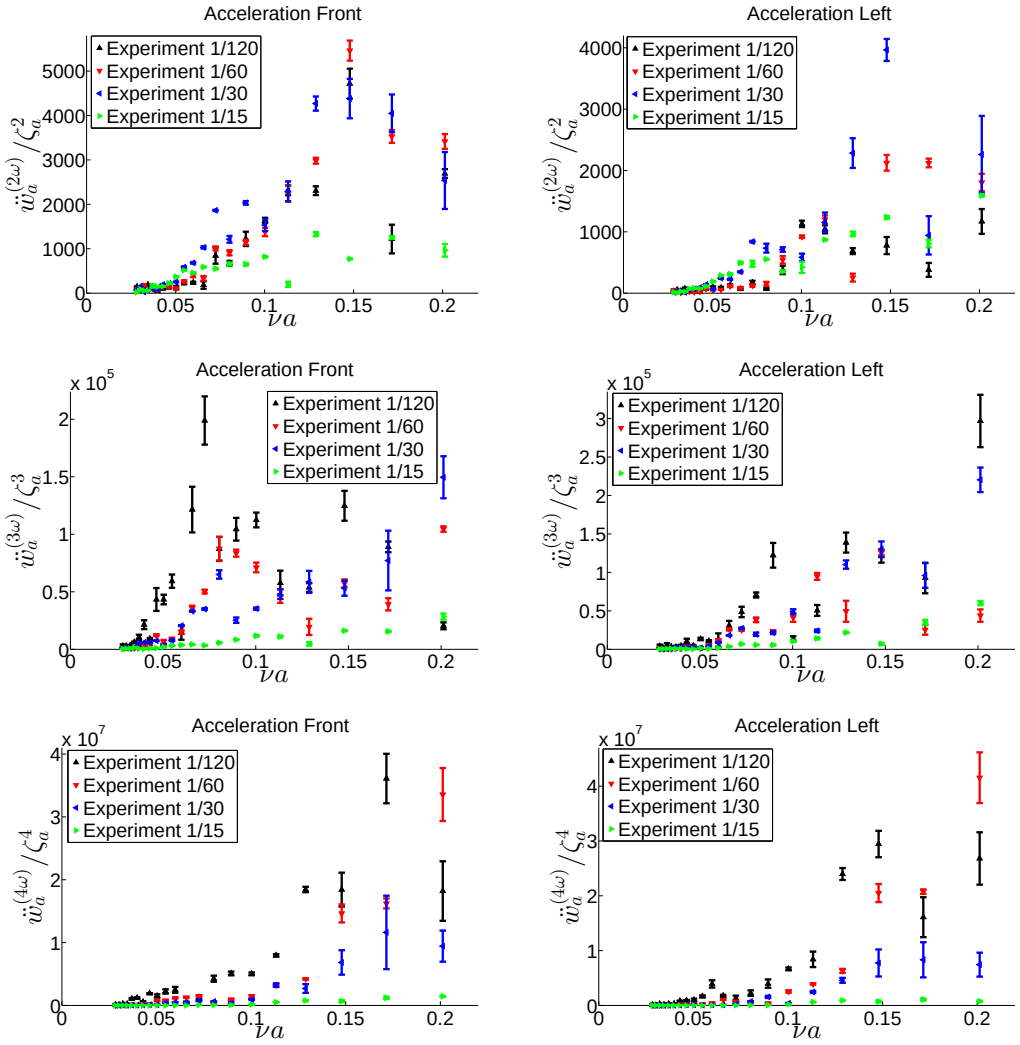

Figure 20: Steady-state amplitudes of experimental non-dimensional second-harmonic acceleration $\ddot{w}_a^{(2\omega)}/\zeta_a^2$, third-harmonic acceleration $\ddot{w}_a^{(3\omega)}/\zeta_a^3$ and fourth-harmonic acceleration $\ddot{w}_a^{(4\omega)}/\zeta_a^4$ along body-fixed $\overline{z}$-axis versus non-dimensional wave number νa for wave height-to-wavelength ratios $1/120, 1/60, 1/30$ and $1/15$ for floater front position ($\beta = \pi$) and left position ($\beta = \pi/2$) in incident regular waves with frequency ω and amplitude ζ_a. The height of the experimental error bars is two times the estimated standard deviation.

approach in seakeeping analysis of ships by calculating correctly nonlinear Froude-Kriloff forces and unsteady hydrostatic forces in nonlinear incident waves together with linear hydrodynamic forces. However, we could not explain the experimental results by following such an approach. The fact that part of the torus may go out of the water in cases with overtopping is also illustrated in Figure 5 together with a photo from a floater of a full scale fish farm without net in a storm illustrating that the same phenomena occur in real life (see Figure 1).

6. Conclusions and future studies

Longitudinal motions and vertical accelerations of a nearly rigid floating torus in regular waves are studied by model tests. The results for the smallest wave height-to-wave length ratios 1/120 are compared with HydroStar, which solves numerically the frequency-domain potential-flow problem correctly to second order in incident wave amplitude for a rigid floater. Reasonable agreement is shown. Experimental and numerical errors are discussed. Differences in the first and second harmonics response are partly explained to be due to hydroelasticity associated with bending stiffness of the floater by using a curved beam theory for the linear problem. Higher order wave-body interaction effects cannot be disregarded. It is documented that viscous effects are secondary. However, tank wall interference matters at the tank's transverse natural sloshing frequencies.

The experimental results for wave steepness $1/120, 1/60, 1/30$ and $1/15$ show that first, second, third and fourth harmonics vertical acceleration of the floater matter in steady-state conditions. We cannot explain the third and fourth harmonics response by a perturbation method with the wave steepness as a small parameter. The torus shape above the mean free surface is likely to matter. Actually, the ratio between the incident wave amplitude and the cross-sectional torus radius ought to be considered as a small parameter.

The experimental and numerical results show that resonant wave motion does not occur inside the torus.

Ideally, we need a fully nonlinear 3D CFD method that accounts for hydroelasticity to compare with the experiments. We say fully nonlinear because the experiments show that even fourth-order harmonics of the measured floater accelerations mattered in steeper waves and that perturbation methods are only practical for linear (first-order) and second-order problems, which accounts only for first and second order harmonics as well as a constant of the floater acceleration in regular waves. In addition, a perturbation method for the third and fourth-order problem becomes questionable as stated above. Difficulties may also arise because of singularities at the contact line between the mean free surface and the torus (Faltinsen and Timokha (2010)). Furthermore, Navier-Stokes equation is needed because flow separation is likely to matter for steeper waves. Use of a fully nonlinear 3D CFD method that accounts for hydroelasticity requires future studies.

Acknowledgement

This work was supported by the Research Council of Norway through the Centres of Excellence funding scheme AMOS, project number 223254.

The free use of HydroStar by Bureau Veritas is acknowledged.

References

Faltinsen, O. M., 1990. Sea Loads on Ships and Offshore Structures. Cambridge University Press, Cambridge, England.

Faltinsen, O. M., Timokha, A. N., 2010. A multimodal method for liquid sloshing in a two-dimensional circular tank. Journal of Fluid Mechanics 665, 457–479.

He, Z., Faltinsen, O. M., Fredheim, A., Kristiansen, T., September 16-19 2015. The influence of fish on the mooring loads of a floating fish farm. In: Proceedings of the 7th International Conference on Hydroelasticity in Marine Technology. Split, Croatia.

Kristiansen, D., Faltinsen, O. M., 2009. Non-linear wave-induced motions of cylindrical-shaped floaters of fish farms. Proceedings of the Institution of Mechanical Engineers, Part M: Journal of Engineering for the Maritime Environment 223, 361–375.

Kristiansen, T., Faltinsen, O. M., 2015. Experimental and numerical study of an aquaculture net cage with floater in waves and current. Journal of Fluids and Structures 54, 1–26.

Li, P., Faltinsen, O. M., October 1-5 2012. Wave induced response of an elastic circular collar of a floating fish farm. In: Proceedings of 10th International Conference on Hydrodynamics. Vol. **2**. St. Petersburg, Russia, pp. 58–64.

Li, P., Faltinsen, O. M., Greco, M., June 8–13 2014. Wave-induced accelerations of a fish-farm elastic floater: experimental and numerical studies. In: Proceedings of the ASME 2014 33rd International Conference on Ocean, Offshore and Arctic Engineering. Vol. **7**. San Francisco, California, USA.

Love, A. E. H., 2013. A treatise on the mathematical theory of elasticity. Cambridge University Press, Cambridge, England.

Newman, J. N., 1962. The exciting forces on fixed bodies in waves. Journal of Ship Research 6 (3), 10–17.

Newman, J. N., 1977. The motion of a floating slender torus. Journal of Fluid Mechanics 83, 721–735.